An extended abstract for the 46th AIAA/ASME/SAE/ASEE Joint Propulsion Conference & Exhibit, July 25-28, 2010, Nashville, Tennessee

Transient Three-Dimensional Side Load Analysis of Out-of-Round Film Cooled Nozzles

Ten-See Wang[*], Jeff Lin[†], Joe Ruf[‡], and Mike Guidos[§]
NASA Marshall Space Flight Center, Huntsville, Alabama, 35812

The objective of this study is to investigate the effect of nozzle out-of-roundness on the transient startup side loads. The out-of-roundness could be the result of asymmetric loads induced by hardware attached to the nozzle, asymmetric internal stresses induced by previous tests and/or deformation, such as creep, from previous tests. The rocket engine studied encompasses a regeneratively cooled thrust chamber and a film cooled nozzle extension with film coolant distributed from a turbine exhaust manifold. The computational methodology is based on an unstructured-grid, pressure-based computational fluid dynamics formulation, and a transient inlet history based on an engine system simulation. Transient startup computations were performed with the out-of-roundness achieved by four degrees of ovalization of the nozzle: one perfectly round, one slightly out-of-round, one more out-of-round, and one significantly out-of-round. The computed side load physics caused by the nozzle out-of-roundness and its effect on nozzle side load are reported and discussed.

Nomenclature

C_1, C_2, C_3, C_μ= turbulence modeling constants, 1.15, 1.9, 0.25, and 0.09.

C_p = heat capacity

---

[*] Aerospace Engineer, ER42, Fluid Dynamics Branch, Propulsion Structure, Thermal, and Fluids Analysis Division, Senior Member AIAA.
[†] Aerospace Engineer, ER42, Fluid Dynamics Branch, Propulsion Structure, Thermal, and Fluids Analysis Division,.
[‡] Aerospace Engineer, ER42, Fluid Dynamics Branch, Propulsion Structure, Thermal, and Fluids Analysis Division.
[§] Aerospace Engineer, ER21, Liquid Engine & Main Propulsion Systems Branch, Propulsion Systems Design & Integration Division.

1

D	= diffusivity
F_{yz}	= integrated force in the lateral direction
H	= total enthalpy
K	= thermal conductivity
k	= turbulent kinetic energy
L/S	= ratio of long axis to short axis
Q	= heat flux
T	= temperature
t	= time, s
u	= mean velocities
V^2	$= \sum u^2$
x	= Cartesian coordinates or nondimensional distance
α	= species mass fraction
ε	= turbulent kinetic energy dissipation rate
θ	= energy dissipation contribution
μ	= viscosity
μ_t	= turbulent eddy viscosity ($=\rho C_\mu k^2/\varepsilon$)
Π	= turbulent kinetic energy production
ρ	= density
σ	= turbulence modeling constants, 0.9, 0.9, 0.89, and 1.15 for Eqs. (2), (4)~(6).
τ	= shear stress
ω	= chemical species production rate

Subscripts

r	= radiation
t	= turbulent flow
w	= wall
∞	= ambient

2

I.   Introduction

Structural damages to the engine and its supporting flight hardware due to nozzle lateral forces during transient operations have been found for almost all liquid rocket engines during their initial development [1-5]. For example, the J-2 engine had its gimbal block retaining bolts failed in tension [5], and the Space Shuttle Main Engine (SSME) had the liquid hydrogen feedline or steerhorn fractured [2,5], and the Japanese LE-7A engine had its cooling tubes broken [4]. And there have been many unreported incidents all over the world. Therefore, transient nozzle side load is always considered a high risk item and a critical design issue during any new engine development.

The J-2X engine, the Ares I upper stage engine under development, is an evolved variation of two historic predecessors: the powerful J-2 engine that propelled the upper stages of the Apollo-era Saturn IB and Saturn V rockets, and the J-2S, a derivative of the J-2 that was developed and tested but never flown, and both have seen the damaging nature of the side forces. Since the asymmetric shock evolutions inside the nozzle, or the origins of the transient nozzle side loads, occur naturally during the nozzle fill up or evacuation processes, it can be safely assumed that the J-2X engine will experience side forces, just like its predecessors such as J-2 and J-2S, or engines similar in design such as the LE-7A and Vulcain engines.

Several approaches have, therefore, been used to study the J-2X side load under various operating and design conditions, and are continuously being used to explore various possibilities during testing and flight conditions. These approaches range from the empirical or skewed plane approach [5], cold flow testing and scaling [8], and computational fluid dynamics (CFD) and heat transfer analysis approach [9]. One of the potential issues being explored is the effect of deformation, or out-of-roundness of the nozzle.

Liquid rocket engine nozzles, being large with relatively light weight structures, are probably never truly round. The cause of out-of-roundness could be, but are not limited to, the following: asymmetric loads induced by hardware attached to the nozzle, asymmetric material internal stresses induced in previous tests or nozzle wall material deformation, such as creep, incurred in previous engine tests.

Since asymmetric shock revolutions inside the nozzle generate side loads naturally on perfectly round nozzles, questions were raised about the side load characteristics of out-of-round nozzles. The objective of this effort is, therefore, to investigate the effect of nozzle out-of-roundness on the start transient side loads. Since J-2X is an upper

stage engine and the tests will be performed in an altitude test stand that provides a simulated altitude of 100,000 ft, transient 3-D CFD and heat transfer computations were performed for the engine start with a back pressure equivalent to 100,000 ft. Four nozzles with different degrees of ovalization were used to study the effect of out-of-roundness: a perfectly round nozzle or the baseline nozzle, a slightly ovalized nozzle, a more ovalized nozzle, and a significantly ovalized nozzle. The preliminary results of these computations are presented and discussed herein.

II.   Computational Methodology

A. Computational Fluid Dynamics

The CFD methodology is based on a multi-dimensional, finite-volume, viscous, chemically reacting, unstructured grid, and pressure-based formulation. Time-varying transport equations of continuity, species continuity , momentum, total enthalpy, turbulent kinetic energy, and turbulent kinetic energy dissipation were solved using a time-marching sub-iteration scheme and are written as:

$$\frac{\partial \rho}{\partial t} + \frac{\partial}{\partial x_j}\left(\rho u_j\right) = 0 \tag{1}$$

$$\frac{\partial \rho \alpha_i}{\partial t} + \frac{\partial}{\partial x_j}\left(\rho u_j \alpha_i\right) = \frac{\partial}{\partial x_j}\left[\left(\rho D + \frac{\mu_t}{\sigma_\alpha}\right)\frac{\partial \alpha_i}{\partial x_j}\right] + \omega_i \tag{2}$$

$$\frac{\partial \rho u_i}{\partial t} + \frac{\partial}{\partial x_j}\left(\rho u_j u_i\right) = -\frac{\partial p}{\partial x_i} + \frac{\partial \tau_{ij}}{\partial x_j} \tag{3}$$

$$\frac{\partial \rho H}{\partial t} + \frac{\partial}{\partial x_j}\left(\rho u_j H\right) = \frac{\partial p}{\partial t} + Q_r + \frac{\partial}{\partial x_j}\left[\left(\frac{K}{C_p} + \frac{\mu_t}{\sigma_H}\right)\nabla H\right] + \frac{\partial}{\partial x_j}\left[\left(\left(\mu + \mu_t\right) - \left(\frac{K}{C_p} + \frac{\mu_t}{\sigma_H}\right)\right)\nabla\left(V^2/2\right)\right] + \theta \tag{4}$$

$$\frac{\partial \rho k}{\partial t} + \frac{\partial}{\partial x_j}\left(\rho u_j k\right) = \frac{\partial}{\partial x_j}\left[\left(\mu + \frac{\mu_t}{\sigma_k}\right)\frac{\partial k}{\partial x_j}\right] + \rho\left(\Pi - \varepsilon\right) \tag{5}$$

$$\frac{\partial \rho \varepsilon}{\partial t} + \frac{\partial}{\partial x_j}\left(\rho u_j \varepsilon\right) = \frac{\partial}{\partial x_j}\left[\left(\mu + \frac{\mu_t}{\sigma_\varepsilon}\right)\frac{\partial \varepsilon}{\partial x_j}\right] + \rho\frac{\varepsilon}{k}\left(C_1\Pi - C_2\varepsilon + C_3\Pi^2/\varepsilon\right) \tag{6}$$

A predictor and corrector solution algorithm was employed to provide coupling of the governing equations. A second-order central-difference scheme was employed to discretize the diffusion fluxes and source terms. For the convective terms, a second-order upwind total variation diminishing difference scheme was used. To enhance the temporal accuracy, a second-order backward difference scheme was employed to discretize the temporal terms. Point-implicit method was used to solve the chemical species source terms. Sub-iterations within a time step were

used for driving the system of second-order time-accurate equations to convergence. Details of the numerical algorithm can be found in Ref's [18-21].

An extended k-ε turbulence model [22] was used to describe the turbulence. A modified wall function approach was employed to provide wall boundary layer solutions that are less sensitive to the near-wall grid spacing. Consequently, the model has combined the advantages of both the integrated-to-the-wall approach and the conventional law-of-the-wall approach by incorporating a complete velocity profile and a universal temperature profile [23]. A 7-species, 9-reaction detailed mechanism [23] was used to describe the finite-rate, hydrogen/oxygen afterburning combustion kinetics. The seven species are H_2, O_2, H_2O, O, H, OH, and N_2. The thermodynamic properties of the individual species are functions of temperature. The multiphysics pertinent to this study have been anchored in earlier efforts, e.g., SSME axial force and wall heat transfer [18], SSME startup side load [9], J-2X startup and shutdown side loads for a nozzlette configuration [W1], nozzle film cooling applications [24], and conjugate heat transfer [25].
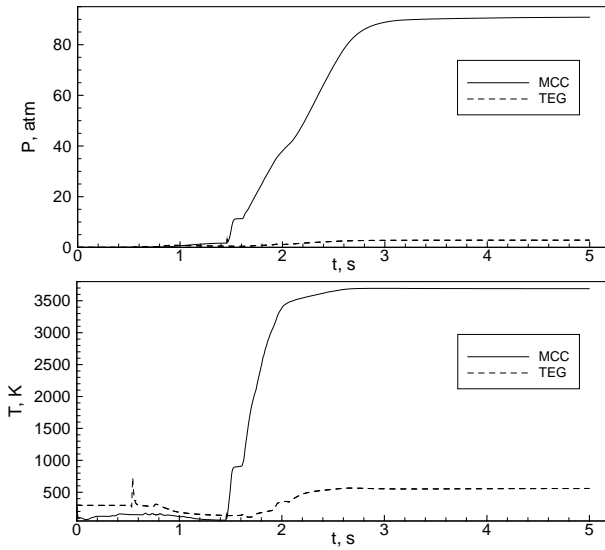

Fig. 1 Simulated inlet pressure and temperature histories for the main combustion chamber and turbine exhaust gas flows during the start-up transient.
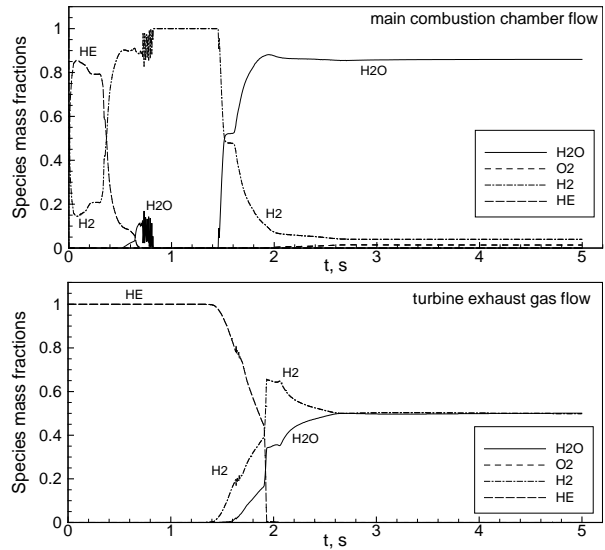
Fig. 2 Simulated inlet species mass fraction histories for the main combustion chamber and turbine exhaust gas flows during the start-up transient.

C. Simulated Startup Sequences

The startup and shutdown sequences are important drivers to the nozzle side load physics [9, W1]. They contain not only the inlet pressure and temperature histories, but also the species mass fraction histories. The ramp rate of the pressure sequence generally determines the magnitude and duration of the peak side load. The temperature and species mass fraction sequences determine the extent of the combustion reactions that in turn affects the magnitude and duration of the peak side load. Another reason the temperature and species composition are important is because they largely determine the specific heat distribution which in turn determine the shock shape, which again impacts the side load physics. Given another example of the importance of the species composition, if excess fuel is dumped at certain period of time, combustion waves could occur and that add to the severity of the side load.

System-level modeling is an important tool in the design and planning of sequencing the transient events of rocket engine operation. Transient system-level simulations provide the histories of the aforementioned variables as determined from a lumped, control-volume analysis approach to simulate the network of components and sub-components, including the valve actions, in a rocket engine. Figure 1 shows the inlet pressure and temperature histories, and Fig. 2 shows the inlet species mass fraction histories, for the main combustion chamber (MCC) and the turbine exhaust gas (TEG) flows during the startup transient. TEG flow is used as film coolant for the J-2X engine as well as to provide a small benefit to engine thrust performance. The transient reactant composition obtained from system modeling at the two inlets was preprocessed with the Chemical Equilibrium Calculation program [26], assuming the propellants were ignited to reach equilibrium composition immediately beyond the injector faceplate. It can be seen from Fig. 1 that the MCC pressure and temperature ramps mainly between 1.4 and 3 s. Also, it can be seen from Fig. 2 that immediately following the start command, helium (He) gas enters both the MCC, via purge flow, and the TEG chamber, initially via purge flow but then as flow injected to assist the start-up of the J-2X turbopumps. These He flows effectively dilute the fuel concentration in the early startup process. It was found in an earlier study [W1] that a combination of the fuel dilution and a shorter ramp time than that of the SSME eliminated the occurrence of potentially hazardous combustion wave [9]. It should be pointed out that the startup sequences shown in Figs 1 and 2 are different from those shown in an earlier study [W1], e.g., the temperature spike during the earlier startup transient [W1] was eliminated based on revisions to the J-2X valve sequencing.

III.   Computational Grid Generation

The computational domain for the J-2X out-of-round nozzle side load investigation includes the MCC and nozzle, turbine exhaust manifold (TEM) for TEG flow injection, nozzle extension, plume, and freestream regions. The general procedure of the grid generation follows that of the nozzlette configuration of J-2X side load study effort [W1] by rotating an axisymmetric grid without the TEM, using a software package GRIDGEN [27]. Fig. 3 shows the layout of a typical computational grid. The outer boundaries and the wall boundaries for the MCC, nozzle, nozzlette, and nozzle extension are shown in the top figure. It also shows the positive x-direction is that of the axial flow, hence the
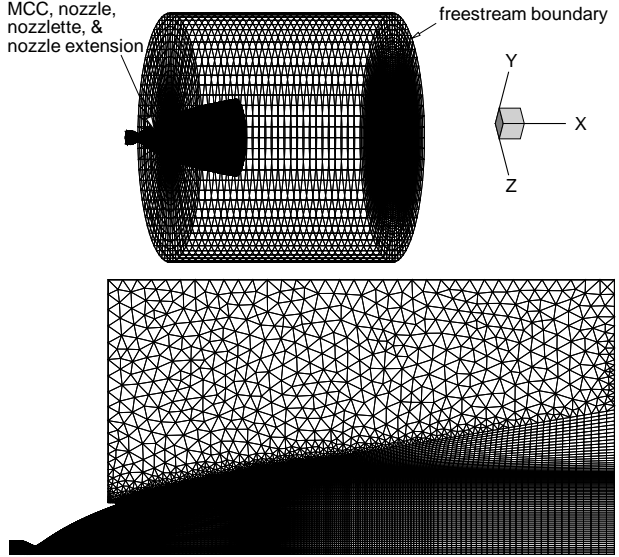

Fig. 3   The layout of a hybrid computational grid. Top: an overall view. Bottom: the axisymmetric grid used to construct the final 3-D grid.
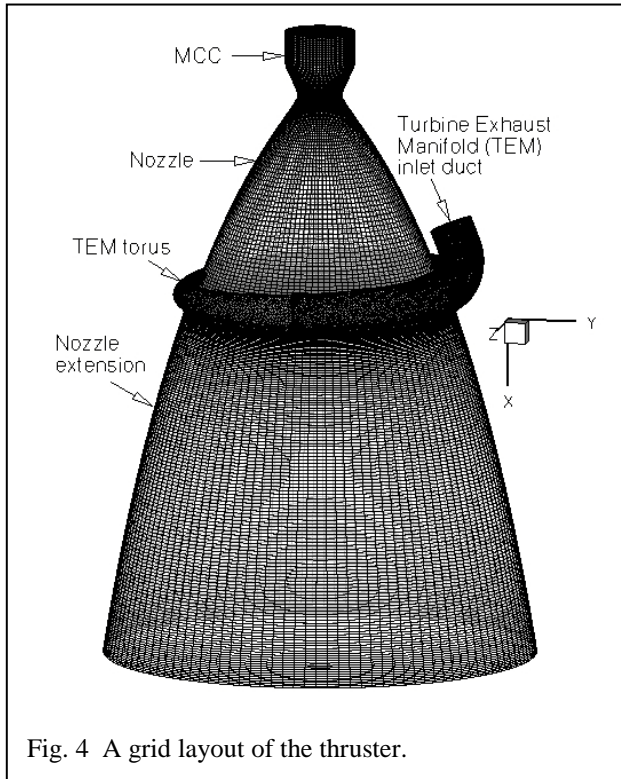
aerodynamic forces exerted in the y- and z- directions are the side forces. The TEM grid was constructed separately. The final grid was completed by merging the two grids.

Both the nozzlette and TEM are used to supply film coolant into the nozzle extension. The difference between the two configurations is the that nozzlette geometry is symmetric to the thruster centerline, implying uniform mass flow distribution circumferentially, while the TEM is a torus and not symmetric to the thruster centerline and implying a non-uniform mass flow distribution in the circumferential direction. Figure 4 shows a typical grid layout of the thruster with the current TEM configuration. Once can see the TEM consists of an inlet duct and a torus with which the

Fig. 4 A grid layout of the thruster.

incoming TEG flow is split under the inlet duct and flow around the torus to enter the nozzle extension. The torus has a tapered flow area from just under the inlet duct all the way to the opposite end. The tapered flow area was intended to make the film coolant to distribute more uniformly as it enters the nozzle extension. However, for this particular TEM configuration, a separate steady-state analysis indicated a 9% variation in mass flow distribution from the inlet duct side to the opposite side.

Figure 5 shows a close-up view of the TEM without the nozzle extension attached. It can be seen that the film coolant flow comes in from the TEM inlet duct, splits and flows around the TEM torus and over the structural ribs, and finally entering the nozzle extension through the TEG exit ring as a barrier to protect the nozzle extension wall.

Fig. 5   A close-up view of the turbine exhaust manifold.
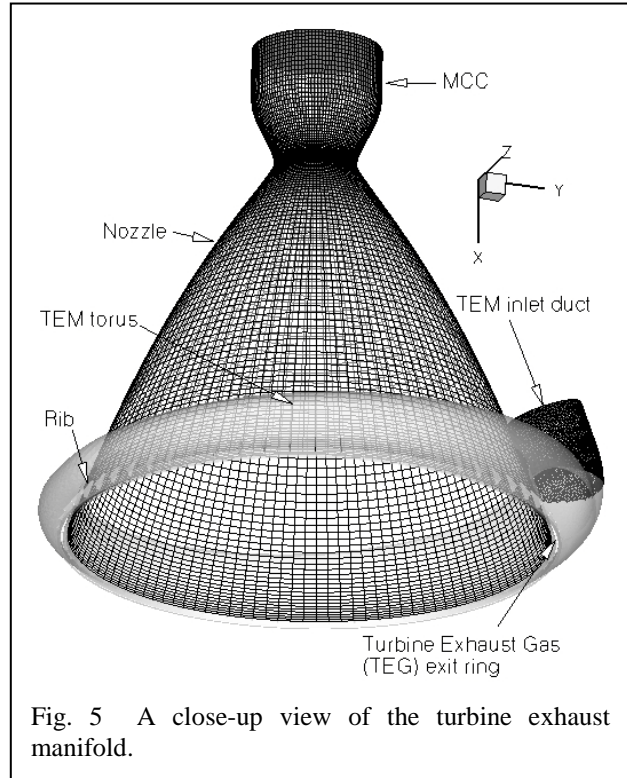
The grid layouts shown in Figs 4 and 5 are for the perfectly round, or the nominal case. The non-roundness of the thruster is achieved by ovalizing the thruster. Figure 6 shows a cross-sectional view of the four thrusters generated for this study. The out-of-roundness of the thruster is measured by the ratio of the length of the long axis to that of the short axis, or L/S. The nominal, or the perfectly round case, has L/S ratio of equaling unity; the slightly out-of-round case, or Case 1, has a L/S ratio of 1.0086; the more out-of-round case, or Case 2, has a L/S ratio of 1.0346. Then there is the significantly out-of-round case, or Case 3 that has a high L/S ratio of 1.4400. It is anticipated that the slightly out-of-round and the more out-of-round cases are likely the result of previously mentioned stresses, while the significantly out-of-round Case 3 is a hypothetical case that was designed as the worst or the most conservative case, such that the nozzle side load physics might be magnified. The long axis is assumed to be aligned in the z-direction, hence the short axis is aligned in the y-direction. The total number of grid points is 3,653,299, or 4,421,166 cells for all four cases. The total cell numbers used in this study is higher than the 2,058,192 cells used in the nozzlette configuration [W1], and much higher than the 1,275,120 cells used in the SSME benchmark [9], and the 145,500, 145,500, and 405,900 points used on LE-7, LE-7A, and CTP50-R5-L [10], and the 85,000 cells used on Vulcain 2 [11], respectively. It is noted that although the cross-sectional flow areas of the four thrusters do not have to be the same, they are kept the same such that the results are compared based on the same flow area.
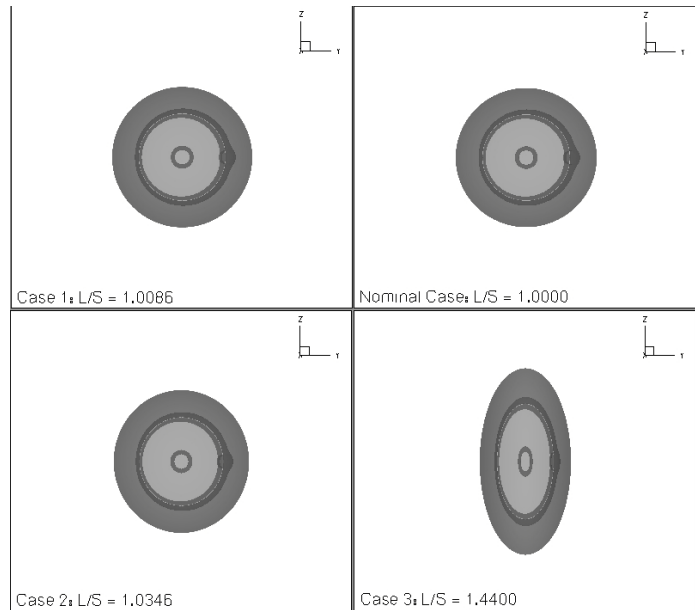

Fig. 6   Cross-sectional view of the ovalized nozzles.

IV.   Boundary and Inlet Conditions

Fixed total conditions were used for the freestream boundaries. Time-varying inlet flow boundary conditions were used at the inlets for the MCC and TEG flows. These time-varying inlet flow properties were obtained from the system simulations that include the time varying total pressure, temperature, and reactant composition, as shown in Figs. 1-2. The details about the system simulations are discussed earlier. For startup computations, the thermal wall boundary condition was started out as adiabatic. As the startup transient reaches 1.4 s, when the MCC temperature starts to ramp up, as shown in Fig. 1, wall temperature profiles obtained from separate steady-state calculations were imposed onto the thruster walls, as discussed in [9, W1]. Since J-2X is the Ares I upper stage engine under development, all cases reported herein were computed at an ambient pressure corresponding to 100,000 ft.

V.   Preliminary Results and Discussion

The computations were performed on a cluster machine using 10~16 processors. Global time steps were varied throughout the computations: 2.5~10 μs were typically used during the initial transient when the change of flow physics was mild, and 1~2.5 μs were used when strong flow physics such as combustion, shock transitions and separation line jumping over the TEG exit were occurring. These time steps correspond to CFL numbers ranging approximately from 0.1 to unity.

A. The Nominal Case

Figure 7 shows the computed J-2X side load histories for the startup transients at altitudes of 100k ft. Following the description of the physics occurring at different time periods in Fig. 7, the exhaust plume starts out as a subsonic core jet flow. As the chamber pressure increases, the core jet flow strengthens and it becomes supersonic and a Mach disk develops near the throat at around 0.40 s. At this moment the supersonic core jet below the Mach disk still looks like a solid jet. Immediately thereafter though, a flow recirculation starts to form beneath the disk and we have a cone-like supersonic jet. This initial Mach disk flow is separated from the nozzle wall from the throat down, just like the earlier core jet flow.

10

As the Mach disk flow develops continuously and the size of the Mach disk grows, it imposes an adverse pressure gradient on the nozzle wall. As the wall boundary layer not able to negotiate this adverse pressure gradient
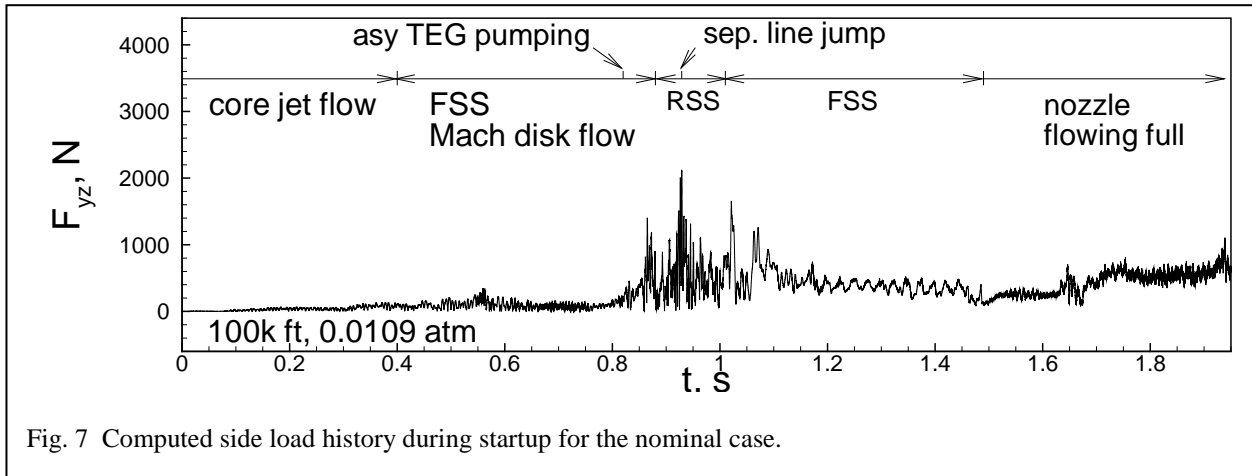

Fig. 7 Computed side load history during startup for the nominal case.

due to wall friction, the Mach disk flow stays separated, resulting in an oblique shock foot (shock stem) coming off the wall, intersecting the Mach disk and the detached supersonic jet at the triple point. Since the shock and separated flow pattern of this detached, hollow supersonic jet flows freely and away from the wall, it is referenced as a free-shock separation (FSS) [1]. This developing and advancing FSS Mach disk flow is best described by snapshots of time-varying Mach number contours and separation lines (not shown).

Since the ambient pressure at 100k ft is 0.0109 atm, the external environment behaves effectively as a vacuum pump, drawing both the engine Mach disk and TEG flows out of the thruster faster than that at sea level. On the other hand, The Mach disk flow and TEG flow are also trying to influence each other as they establish themselves in the nozzle. Unlike the case of the uniform mass flow nozzlette configuration [W1], in which a slight imbalance in the circumferential wall pressure between the TEG exit and the Mach disk flow separation line, caused by the almost symmetric TEG pumping, caused the Mach disk flow to become asymmetric. With the TEM configuration, by nature most of the TEG flow naturally comes in under the inlet duct end than the opposite end, especially during the transient startup. As a result, the supersonic jet was sucked towards the inlet duct end, followed by a slanted separation line and then the whole Mach disk flow moving towards the stronger suction side, and a first side load jump. Because the TEG flow in the TEM configuration emerges asymmetric to start with, it is referred to as the asymmetric TEG pumping. At about 0.88 s into the transient, the supersonic jet is draw to merge with the TEG flow to form the flow pattern of the restricted shock separation (RSS) [1], induced by the pumping force of the TEG flow. At about 0.929 s into the transient, a peak side load occurs due to the jump of the separation line over the TEG exit

ring. Jump of the separation line [W1], also known as the jump of the separation point [4], is the interaction of the rear shock stem with the TEG flow and the TEG flow exit ring which usually produces the peak side load for a film cooled engine. Around 1.01 s into the transient, the reattachment line steps out of the nozzle extension and we have another local side load jump and the corresponding physics is dubbed as the RSS-to-FSS transition. After which the separation line moves up towards the TEM torus and then moves down at around 1.085s. The separation line eventually moves out the nozzle extension at around 1.49 s and the nozzle is flowing full. At that time we have an over-expanded full flowing flow which potentially will give the highest buckling load.
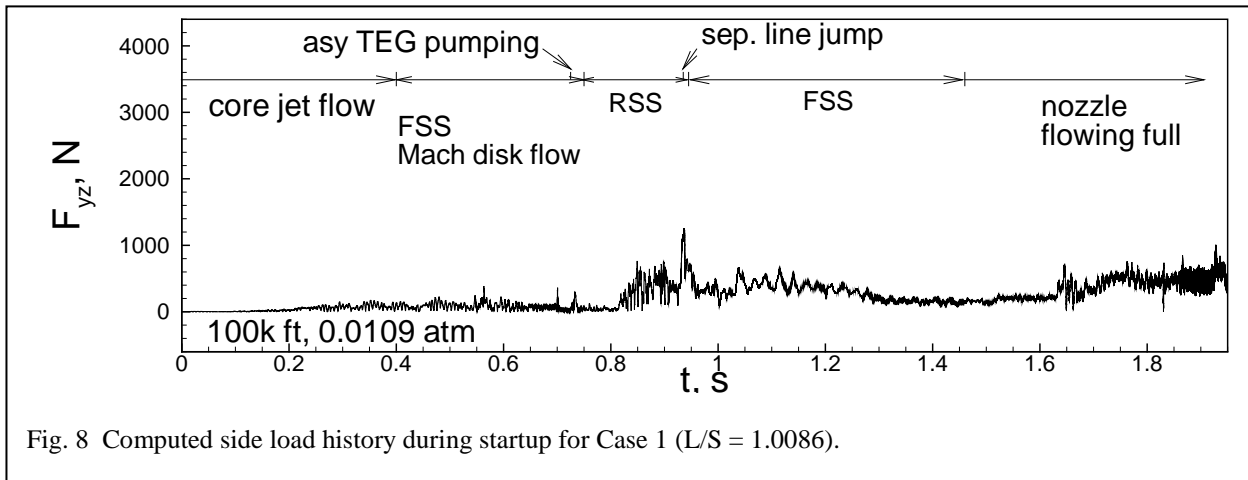

Fig. 8 Computed side load history during startup for Case 1 (L/S = 1.0086).

B. Out-of-round Cases

The physics occurring during the startup of the first two out-of-round cases are similar to those of the nominal case. That is, a core jet flow starts out the initial startup process. It then develops into a FSS Mach disk flow. Sometime during that FSS Mach disk flow progression, the naturally occurring uneven TEG flow mass distribution around the torus duct causes the asymmetric TEG flow pumping. A short while later the FSS transits into RSS. Near the end of the RSS Mach disk flow advancement, separation line jumps over the TEG flow inlet back-step formation, generating a peak side load. Subsequently, after which the RSS falls back to FSS and eventually the nozzle flows full. The occurring time and residence time of those physics are presented in Figs 8 and 9, in which the computed side load histories are shown for Case 1 (L/S = 1.0086) and Case 2 (L/S = 1.0346), respectively. Comparing to those shown in Fig. 7, there appears to be a mysterious stabilizing effect occurring in the slightly out-of-round Case 1 and more out-of-round Case 2 such that the asymmetric pumping and the FSS-to-RSS transition did not cause discernible local side load jumps, as those of the perfectly round case. The separation line jump does
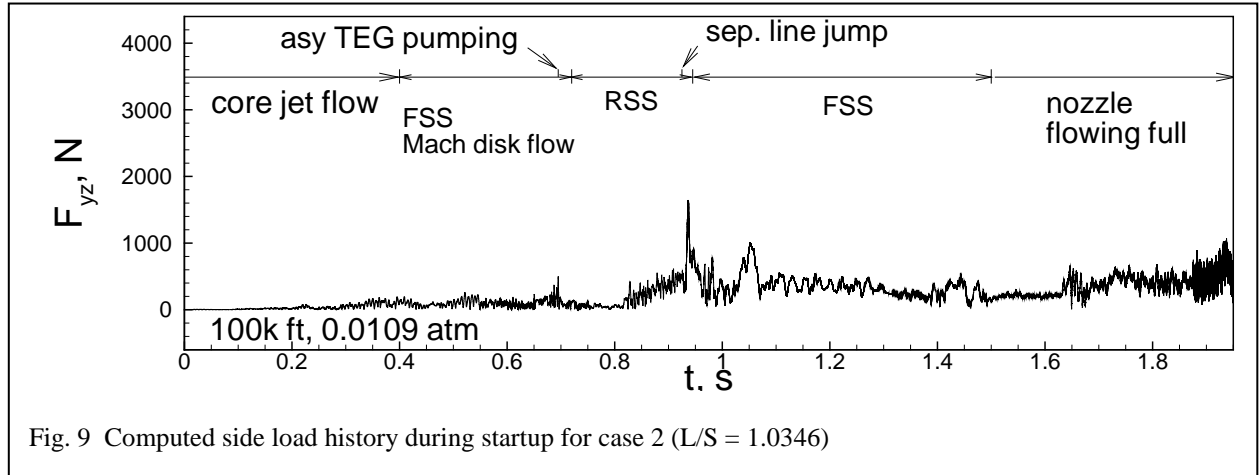
Fig. 9 Computed side load history during startup for case 2 (L/S = 1.0346)

generate side load jumps for both out-of-round cases, although the resulting peak side loads for the two cases are lower than that of the nominal case. The local side load jumps due to RSS-to-FSS transition for the two out-of-round cases are also appear to be delayed or muffed.

Examining the event occurring time of the flow physics, it appears that the starting times of the asymmetric TEG pumping and the shock transitions are earlier than those of the nominal case. This observation is summarized in Table 1.

Table 1.   A comparison of the computed flow physics occurring time

Elapsed time, s	Core jet to FSS	Asymmetric TEG pumping	RSS	Sep line jump	FSS	Flowing full
nominal	0.400	0.820	0.88	0.929	1.010	1.49
Case 1	0.400	0.725	0.75	0.935	0.945	1.46
Case 2	0.400	0.695	0.72	0.925	0.945	1.50
Case 3	0.395	0.550	0.855 (PRSS & RSS)	0.930	0.950	1.50

Figure 10 shows the computed side load history and the event occurring and residence times of the physics for the significantly out-of-round Case 3. Although the physics in general appear to be similar to those of the prior three cases, the flow physics actually look fairly different in the scalar contours views (not shown). For example, a significant difference in the flow physics for Case 3, comparing to the prior three cases, is that after the FSS-to-RSS transition, instead of staying as RSS for a period of time, there are many jumping back-and-forth between RSS and partial RSS (PRSS). It is noted that for L/S = 1.4400, when the nozzle is so much ovalized, it is almost crashed on one side. In addition, we note that if the ratio of the long axis to the short axis was infinitely long, the flow inside the
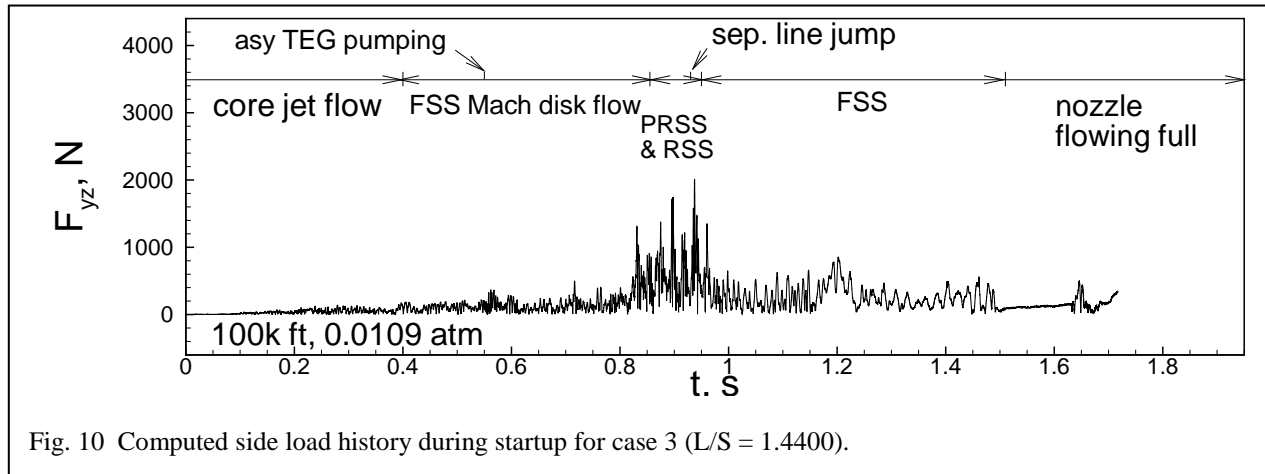
13

Fig. 10 Computed side load history during startup for case 3 (L/S = 1.4400).

thruster will look like a two-dimensional flow, instead of a three-dimensional flow. Another interesting observation is that the event occurring for the FSS-to-RSS transition, comparing to that of the two prior two non-round cases, is delayed to 0.855 s, and almost close to the 0.88 s of the nominal case, as shown in Table 1. Furthermore, Case 3 has all the local side load jumps due to the transition in physics, but the magnitudes are not higher than those of the nominal case, in spite of the significantly overalized cross section.

VI.   Summary

Three-dimensional numerical investigations on the transient startup process have been performed to study the effect of out-of-roundness of nozzle on the nozzle side load physics. Four cases have been computed or being computed: one nominal case or a perfectly round case as the baseline, one slightly out-of-round case, one more out-of-round case, and one significantly out-of-round case. The significantly out-of-round case is still being computed but will be finished soon. Intuitively, it is anticipated that the out-of-round nozzles would produce higher side loads than that of the perfectly round nozzle. Instead, the preliminary results show a surprising flow stabilizing effect from the out-of-round nozzles. As such, the peak side loads of the slightly out-of-round and the more out-of-round cases are lower than that of the nominal case. Even the peak side load of the significantly out-of-round case is not higher than that of the perfectly round case, in spite of its significantly deformed cross section. More data reduction is being performed to explain these unexpected results.

Acknowledgments

References

[1] Nave, L.H., and Coffey, G.A., "Sea Level Side Loads in High-Area-Ratio Rocket Engines," AIAA Paper 73-1284, Nov. 1973.

[2] Cikanek, H.A., "Characteristics of Space Shuttle Main Engine Failures," AIAA Paper 87-1939, June 1987.

[3] Hagemann, G., Terhardt, M., Frey, M., Reijasse, P., Onofri, M., Nasuti, F., and Ostlund, J., "Flow Separation and Side-Loads in Rocket Nozzles," 4th International Symposium on Liquid Space Propulsion, March 12-15, 2000, DLR Lampoldshausen, pp. 1-19.

[4] Watanabe, Y., Sakazume, N., and Tsuboi, M., "LE-7A Engine Nozzle Problems During the Transient Operations," AIAA Paper 2002-3841, July 2002.

[5] Shi, J., "Rocket Engine Nozzle Side Load Transient Analysis methodology – A Practical Approach," AIAA Paper 2005 – 1860, April 2005.

[6] Winterfeldt, L., Laumert, B., Tano, R., Geneau, J.F., Blasi, R., and Hagemann, G., "Redesign of the Vulcain 2 Nozzle Extension," AIAA Paper 2005-4536, Tucson, AZ (2005)

[7] Larson, E.W., Ratekin, G.H., and O'Connon, G.M., "Structural Response to the SSME Fuel Feedline to Unsteady Shock Oscillations," Part 2, Bulletin 52, The Shock and Vibration Bulletin, May 1982, pp. 177-182.

[8] Ruf, J., McDaniels, D.M., and Brown, A.M., "Nozzle Side Load Testing and Analysis at Marshall Space Flight Center," AIAA Paper 2009-4856, July 2009.

[9] Wang, T.-S., "Transient Three-Dimensional Startup Side Load Analysis of a Regeneratively Cooled Nozzle," *Shock Waves – An International Journal on Shock Waves, Detonations and Explosions.* Vol. 19, Issue 3, 2009, pp. 251~264. DOI: 10.1007/s00193-009-0201-2.

[10] Wonezawa, K., Yokota, K., Tsujimoto, K., Sakazume, N., and Watanabe, Y., "Three-Dimensional Unsteady Flow Simulation of Compressed Truncated Perfect nozzles," AIAA Paper 2002-3991, July 2002.

[11] Boccaletto, L., and Lequette, L., "CFD Computation for Rocket Engine Start-Up Simulation," AIAA Paper 2005-4438,

July 2005.

[12] Deck S., and Guillen, P., "Numerical Simulation of Side loads in an Ideal Truncated Nozzle," *Journal of Propulsion and Power,* Vol. 18, No. 2, 2002, pp. 261-269.

[13] Shimizu, T., Miyajima, H., and Kodera, M., "Numerical Study of Restricted Shock Separation on a Compressed Truncated Perfect Nozzle," *AIAA Journal*, Vol. 44, No. 3, 2006, pp. 576-584.

[14] Boccaletto, L., Reijasse, Ph., and Dussauge, J.P., "Dynamic Behaviour of a Separation Oblique Shock During Film Cooling Transient Injection," AIAA Paper 2007-4003, June 2007.

[15] Boccaletto, L., Reijasse, Ph., and Dussauge, J.P., "Influence of Film Cooling Injection on Transient Side Loads," AIAA Paper 2007-5474, July 2007.

[16] Reijasse, Ph., and Boccaletto, L., "Influence of Film Cooling on Nozzle Side loads," AIAA Paper 2008-392, Jan. 2008.

[17] Tomita, T., Takahashi, M., Sasaki, M., Takahashi, M., Tamura, H., Watanabe, Y., and Tsuboi, M., " Parametric Study on the Influence of a Discontinuous Step in a Nozzle Contour on Side-Load," AIAA Paper 2003-4764, July 2003.

[18] Wang, T.-S., "Multidimensional Unstructured-Grid Liquid Rocket Engine Nozzle Performance and Heat Transfer Analysis," *Journal of Propulsion and Power,* Vol. 22, No. 1, January-February, 2006, pp. 78-84.

[19] Shang, H.M., and Chen, Y.-S., "Unstructured Adaptive Grid method for Reacting Flow Computation," AIAA Paper 1997-3183, July 1997.

[20] Wang, T.-S., Chen, Y.-S., Liu, J., Myrabo, L.N., and Mead, F.B. Jr., "Advanced Performance Modeling of Experimental Laser Lightcraft," *Journal of Propulsion and Power,* Vol. 18, No. 6, 2002, pp. 1129-1138.

[21] Chang, G., Ito, Y., Ross, D., Chen. Y.-S., Zhang S., and Wang, T.-S., "Numerical Simulations of Single Flow Element in a Nuclear Thermal Thrust Chamber" AIAA Paper 2007-4143, June 2007.

[22] Chen, Y.-S., and Kim, S. W., "Computation of Turbulent Flows Using an Extended k-ε Turbulence Closure Model," NASA CR-179204, Oct. 1987.

[23] Wang, T.-S., Droege, A., D'Agostino, M., Lee, Y.-C., and Williams, R., "Asymmetric Base-Bleed Effect on X-33 Aerospike Plume Induced Base-Heating Environment," *Journal of Propulsion and Power,* Vol. 20, No. 3, 2004, pp. 385-393.

[24] Chen, Y.-S., Cheng, G.C., and Farmer, R.C., "Reacting and Non-Reacting Flow Simulation for Film Cooling in 2-D Supersonic Flows," AIAA Paper 92-3602, July 1992.

[25] Wang, T.-S., Canabal, F., Chen, Y.-S., and Cheng, G.C., "Multiphysics Computational Analysis of a Solid-Core Nuclear Thermal Engine Thrust Chamber," AIAA Paper 2007-7144, June 2007.

[26] Svehla, R.A., and McBride, B.J., "FORTRAN IV Computer Program for Calculation of Thermodynamic and Transport Properties of Complex Chemical Systems," NASA TN D-7056, Jan. 1973.

[27] Steinbrenner, J.P., Chawner, J.R., and Fouts, C., "Multiple Block Grid Generation in the interactive Environment," AIAA Paper 90-1602, June 1990.

[28] Huynh, H.T., "Analysis and Improvement of Upwind and Centered Schemes on Quadrilateral and Triangular Meshes," AIAA Paper 2003-3541, June 2003.

[29] Coanda, H., "Device for Deflecting a Stream of Elastic Fluid Projected into an Elastic Fluid," US Patent # 2,052,869, Sept. 1, 1936.

[30] Kwan, W., and Stark, R., "Flow Separation Phenomena in Subscale Rocket Nozzles," AIAA Paper 2002-4229, July 2002.

[31] Tomita, T., Sakamoto, H., Onodera, T., Sasaki, M., Takahashi, M., Tamura, H., and Watanabe, Y., "Experimental Evaluation of Side Load Characteristics on TP, CTP, and TO Nozzles," AIAA Paper 2004-3678.

[W1] Wang, T.-S., and Guidos, M., "Transient Three-Dimensional Side Load Analysis of a Film-Cooled Nozzle," to appear in *Journal of Propulsion and Power,* Vol. 25, No. 6, 2009. DOI: 10.2514/1.41025.